Monthly Notices
of the
ROYAL ASTRONOMICAL SOCIETY

MNRAS **498,** 4303–4315 (2020)
Advance Access publication 2020 September 7

doi:10.1093/mnras/staa2705

AMICO galaxy clusters in KiDS-DR3: galaxy population properties and their redshift dependence

Mario Radovich,[1⋆] Crescenzo Tortora,[2,3] Fabio Bellagamba,[4,5] Matteo Maturi,[6,7] Lauro Moscardini,[4,5,8] Emanuella Puddu,[2] Mauro Roncarelli,[4,5] Nivya Roy,[9] Sandro Bardelli,[5] Federico Marulli,[4,5,8] Mauro Sereno,[4,8] Fedor Getman[2] and Nicola R. Napolitano[2,9]

[1] *INAF – Osservatorio Astronomico di Padova, vicolo dell'Osservatorio 5, I-35122 Padova, Italy*
[2] *INAF – Osservatorio Astronomico di Capodimonte, Salita Moiariello 16, I-80131 Napoli, Italy*
[3] *INAF – Osservatorio Astrofisico di Arcetri, Largo Enrico Fermi 5, I-50125 Firenze, Italy*
[4] *Dipartimento di Fisica e Astronomia – Alma Mater Studiorum Università di Bologna, via Piero Gobetti 93/2, I-40129 Bologna, Italy*
[5] *INAF – Osservatorio di Astrofisica e Scienza dello Spazio di Bologna, via Piero Gobetti 93/3, I-40129 Bologna, Italy*
[6] *Zentrum für Astronomie, Universitatät Heidelberg, Philosophenweg 12, D-69120 Heidelberg, Germany*
[7] *ITP, Universität Heidelberg, Philosophenweg 16, D-69120 Heidelberg, Germany*
[8] *INFN – Sezione di Bologna, viale Berti-Pichat 6/2, I-40127 Bologna, Italy*
[9] *School of Physics and Astronomy, Sun Yat-sen University Zhuhai Campus, Daxue Road 2, 519082 Tangjia, Zhuhai, Guangdong, P.R. China*

Accepted 2020 August 29. Received 2020 August 28; in original form 2020 April 9

ABSTRACT

A catalogue of galaxy clusters was obtained in an area of 414 deg^2 up to a redshift $z \sim 0.8$ from the Data Release 3 of the Kilo-Degree Survey (KiDS-DR3), using the Adaptive Matched Identifier of Clustered Objects (AMICO) algorithm. The catalogue and the calibration of the richness–mass relation were presented in two companion papers. Here, we describe the selection of the cluster central galaxy and the classification of blue and red cluster members, and analyse the main cluster properties, such as the red/blue fraction, cluster mass, brightness, and stellar mass of the central galaxy, and their dependence on redshift and cluster richness. We use the Illustris-TNG simulation, which represents the state-of-the-art cosmological simulation of galaxy formation, as a benchmark for the interpretation of the results. A good agreement with simulations is found at low redshifts ($z \le 0.4$), while at higher redshifts the simulations indicate a lower fraction of blue galaxies than what found in the KiDS-AMICO catalogue: we argue that this may be due to an underestimate of star-forming galaxies in the simulations. The selection of clusters with a larger magnitude difference between the two brightest central galaxies, which may indicate a more relaxed cluster dynamical status, improves the agreement between the observed and simulated cluster mass and stellar mass of the central galaxy. We also find that at a given cluster mass the stellar mass of blue central galaxies is lower than that of the red ones.

Key words: galaxies: clusters: general – galaxies: distances and redshifts – galaxies: evolution.

1 INTRODUCTION

Being the most massive collapsed structures in the Universe, galaxy clusters provide a fundamental tool to study the effect of massive dark matter haloes on the properties of their member galaxies (Wechsler & Tinker 2018) and how they evolve with redshift. A remarkable progress in our understanding of the cluster formation and evolution was achieved in the last decades (see e.g. Dressler 1984; Borgani & Kravtsov 2011; Kravtsov & Borgani 2012), but it is clear that clusters provide a complex environment where a variety of physical processes take place, such as star formation, active galactic nucleus feedback, tidal stripping: this is particularly true for the galaxy located at the centre of the cluster halo (De Lucia & Blaizot 2007; Martizzi et al. 2014), which is often, but not always (Hoshino et al. 2015; Hikage et al. 2018), the brightest cluster galaxy (BCG). Cluster formation hierarchical models (see e.g. De Lucia & Blaizot 2007; Moster et al. 2010; Kravtsov & Borgani 2012; Kravtsov, Vikhlinin & Meshcheryakov 2018; Girelli et al. 2020) predict a strong connection between the cluster halo and its BCG. In this scenario, the stellar mass of the BCG is closely related to the mass of the dark matter halo in which it formed, with the most massive haloes hosting the most massive BCGs: as the BCG continues to grow through merging with the surrounding satellite galaxies, its size, luminosity, and stellar mass, as well as the magnitude difference with respect to other nearby cluster members, increase (see Bernardi et al. 2007; e.g. Von Der Linden et al. 2007; Erfanianfar et al. 2019). On the other hand, it is now becoming clear that large-scale environment also plays an important role: clusters with a disturbed dynamical status due to major mergers with smaller clusters have revealed to be more frequent than expected from previous observations (Wen & Han 2013). Mergers are predicted to increase the cluster mass (Lopes et al. 2018) and possibly modify the relation between the cluster halo and BCG mass (Lavoie et al. 2016; Lopes et al. 2018) observed in relaxed clusters, and affect the BCG luminosity in particular at high redshifts (Zenteno et al. 2020).

⋆ E-mail: mario.radovich@inaf.it

Published by Oxford University Press on behalf of the Royal Astronomical Society

Recent cosmological hydrodynamic simulations such as those provided by the Illustris Project (Vogelsberger et al. 2014; Nelson et al. 2015) and its latest release, Illustris-TNG (Marinacci et al. 2018; Naiman et al. 2018; Nelson et al. 2018, 2019; Pillepich et al. 2018b; Springel et al. 2018) are now enabling the possibility to match reasonably well the cluster observables, thanks to the combination of large volume and high particle resolution, even if they may not be yet able to describe all the complex physical processes that shape clusters (see e.g. Barnes et al. 2018).

On the side of observations, wide-field surveys such as the Sloan Digital Sky Survey (SDSS; York et al. 2000), the Kilo-Degree Survey (KiDS; de Jong et al. 2013), the Dark Energy Survey (DES; Dark Energy Survey Collaboration et al. 2016), the Hyper Suprime-Cam Survey (HSC; Aihara et al. 2018), provide multiwavelength photometry of galaxies in individual clusters: the selection of a well controlled but statistically significant number of clusters in a wide range in mass and redshift is required to study in detail how this complex interplay of physical phenomena takes place. This enables us to understand if and how different observables (e.g. the cluster halo mass, the brightness of the central galaxy, star formation in galaxy clusters versus the distance from the cluster centre, etc.) are related, and how they evolve in cosmic time.

Several algorithms to efficiently search for galaxy clusters have been developed (see e.g. Euclid Collaboration 2019, and references therein for a recent review), based either on the fact that early-type galaxies occupy a well-defined position (the red sequence) in the colour–magnitude space at the cluster redshift (e.g. *redMaPPer* and CAMIRA: Rykoff et al. 2014; Oguri et al. 2018, respectively), or on the detection with optimal matched filters (see e.g. Bellagamba et al. 2011) of the galaxy overdensities that are the signatures of galaxy clusters. These produced different catalogues of clusters, allowing to study the properties of their member galaxies (see e.g. Wen & Han 2018; Nishizawa et al. 2018; Sarron et al. 2018; To et al. 2020), though a comparison of the results is challenging due to the different survey properties (area and depth) and algorithm selections.

The Adaptive Matched Identifier of Clustered Objects (AMICO) algorithm (Bellagamba et al. 2018) was used to search for galaxy clusters in the KiDS (Radovich et al. 2017; Maturi et al. 2019). This algorithm does not make an explicit use of colours, in contrast to algorithms based on the detection of a red sequence. This is of great benefit when studying the galaxy population of clusters because the sample selection is not so determined by a specific set of galaxies, allowing for instance to detect clusters with bluer populations. In this paper we analyse the fraction of red and blue galaxies in the KiDS-AMICO clusters and its dependence on cluster mass and redshift, and the properties of red and blue BCGs. In a separate paper (Puddu et al., submitted), we address the dependence of the red and blue cluster galaxies luminosity function on redshift and mass.

The paper is structured as follows. A short summary of the KiDS data set and of the KiDS-AMICO cluster catalogue is given in Sections 2 and 3, respectively. Section 3 also provides a description of the method adopted for the selection of the BCG, and of the validation, based on available spectroscopic redshifts, of the AMICO membership probabilities. Section 4 describes the selection of the red and blue cluster members and their fractions as a function of redshift and distance from the cluster centre are discussed, and compares the KiDS-AMICO and *redMaPPer* cluster detections in the same areas and within the same cluster mass and redshift range. The properties of the BCGs, such as their luminosity and stellar mass are described in Section 5. Section 6 compares the results obtained in this paper with the Illustris-TNG300-1 simulations. Results are summarized and discussed in Section 7.

The cosmology concordance model was adopted throughout the paper: $H_0 = 70$ km s^{-1} Mpc^{-1}, $\Omega_{\rm m} = 0.3$, $\Omega_\Lambda = 0.7$.

2 THE KILO-DEGREE SURVEY

The KiDS (de Jong et al. 2013) is an ESO Public Survey observing with the OmegaCAM camera on the ESO VLT Survey telescope (VST) in the *ugri* bands an area of 1350 deg^2 distributed in two stripes, one equatorial (KiDS-N) and the other towards the South Galactic Pole (KiDS-S). Three main Data Releases are currently available: KiDS-DR2, covering ∼100 deg^2 (de Jong et al. 2015); KiDS-DR3, extending to 440 deg^2 (de Jong et al. 2017); KiDS-DR4 (Kuijken et al. 2019), reaching 1000 deg^2. The supplementary catalogue KV450 (Wright et al. 2019) joined for the first time photometry from KiDS and near-infrared photometry ($ZYJHK_s$) from the parallel ESO Public Survey VISTA Kilo-Degree Infrared Survey (VIKING), for the KiDS-DR3 area. Finally, spectroscopic redshifts for the brightest ($r < 20$ mag) galaxies in KiDS are available through the overlap with the Sloan Digital Sky Survey (SDSS; York et al. 2000) and the Galaxy and Mass Assembly survey (GAMA; Driver et al. 2009) in KIDS-N.

Roy et al. (2018) derived the structural parameters (Sérsic index and effective radius) of the brightest (S/N > 50)[1] galaxies in KiDS-DR2: the Sérsic index and effective size were computed fitting their *gri* images with Sérsic models. The same analysis was extended to KiDS-DR3 and will be presented in a separate paper. In order to select the best-fitting structural parameters, here we imposed the constraint $\chi^2 < 1.3$. As discussed by Roy et al. (2018), larger values of χ^2 correspond to strong residuals, often associated with spiral arms. Moreover, as described by Tortora et al. (2018) stellar masses were computed from *ugri* photometry in KiDS-DR3 using the code LE PHARE (Arnouts et al. 1999; Ilbert et al. 2006), which fits the KiDS photometry to a stellar population synthesis (SPS) theoretical model. Single burst models from Bruzual & Charlot (2003) were used, covering all the range of available metallicities ($0.005 \leq Z/Z_\odot \leq 2.5$), with age smaller than the age of the Universe at the redshift of the galaxy (with a maximum value at $z = 0$ of 13 Gyr) and a Chabrier (2001) IMF. Age and metallicity were left free to vary in the fitting procedure. Models were redshifted using the photometric redshifts derived with the same code, BPZ (Benítez 2000), used to compute photometric redshifts in KiDS. *ugri* magnitudes were measured within a circular aperture of diameter 6 arcsec (and related 1 σ uncertainties δu, δg, δr, and δi) and corrected for Galactic extinction using the map in Schlafly & Finkbeiner (2011). The *r*-band Kron-like magnitudes (MAG_AUTO_r) were used to correct the stellar mass outcomes of LE PHARE for missing flux. Calibration zero-point errors, $(\Delta u_{\rm zp},\ \Delta g_{\rm zp},\ \Delta r_{\rm zp},\ \Delta i_{\rm zp}) = (0.075,\ 0.074,\ 0.029,\ 0.055)$, were added in quadrature to the uncertainties of the magnitudes derived from SEXTRACTOR.

3 THE KiDS-AMICO DR3 CLUSTER CATALOGUE

Differently from other cluster search codes as e.g. *redMaPPer* (Rykoff et al. 2014) and CAMIRA (Oguri et al. 2018), the AMICO algorithm is not based on the detection of the cluster red sequence: instead, an optimal matched filter is applied to a catalogue with

---

[1] Here, the signal-to-noise was defined as the inverse error of *r*-band Kron-like magnitudes in SEXTRACTOR (Bertin & Arnouts 1996): S/N = 1.086/MAGERR_AUTO_r.

coordinates, photometric redshifts and magnitudes, allowing to select galaxy overdensities tracing the presence of galaxy clusters (for details on the algorithm see Maturi et al. 2019, and references therein). The code produces a list of clusters with their centres ($\mathbf{x}$), redshift ($z_{\rm cl}$), significance (SN), and the amplitude (A). For each cluster candidate, a catalogue with the membership probabilities ($p_{\rm memb}$) of galaxies is also available. A first catalogue of galaxy clusters detected in KiDS-DR2 was presented in Radovich et al. (2017). Later, the wider area available in KiDS-DR3 and the new features implemented in the detection algorithm enabled a new analysis, producing a catalogue of 7988 clusters in the redshift range $0.1 < z < 0.8$ over an area of 414 deg^2 after removing areas around bright saturated stars. As described in Maturi et al. (2019), a cut SN > 3.5 was adopted to minimize the number of spurious detections.

3.1 Richness and mass

A full analysis of the properties of this catalogue was presented in Maturi et al. (2019), including the characterization of uncertainties on the AMICO cluster parameters, the evaluation of purity and completeness, and the selection function. Moreover, two new richness parameters (λ and λ^*), derived from the AMICO membership probabilities, were introduced. In particular, the *intrinsic richness* λ^* was designed to reduce its dependence on the redshift, compared to the *apparent richness* λ.

Based on the shear measurements in KiDS-DR3 (Kuijken et al. 2015; Hildebrandt et al. 2017), Bellagamba et al. (2019) made a weak lensing stacked analysis to calibrate the relation between λ_* and the cluster mass M_{200}, defined as the mass within the radius R_{200} where the mean density is 200 the critical density of the Universe at that redshift (equation 31 in Bellagamba et al. 2019):

$$\log \frac{M_{200}}{10^{14} M_{\odot} h^{-1}} = \alpha + \beta \log \frac{\lambda^*}{\lambda^*_{\rm piv}} + \gamma \log \frac{E(z)}{E(z_{\rm piv})}, \quad (1)$$

where $E(z) = H(z)/H_0$, $\alpha = 0.004 \pm 0.038$, $\beta = 1.71 \pm 0.08$, $\gamma = -1.33 \pm 0.64$, $\lambda^*_{\rm piv} = 30$, and $z_{\rm piv} = 0.35$.

3.2 Selection of the BGC

Identifying the central galaxies in clusters is fundamental as their position at the centre of the dark matter haloes from which the cluster formed leads to peculiar properties compared to the other cluster galaxies. However, as discussed by e.g. Hoshino et al. (2015) and Hikage et al. (2018), the cluster central galaxy does not necessarily coincide with the brightest galaxy in the cluster. For this reason, we consider not only the galaxy luminosity, but also its distance from the initial AMICO centre and the membership probability to select the BCG. This is done as follows. For each cluster, we first compute the characteristic magnitude m_* (see Fig. 1), defined as the absolute r-band magnitude $M_r^*(z = 0.1) - 5\log h$, where $M_r^*(z = 0.1) = -20.44$ (Blanton et al. 2003), transformed to the observed apparent magnitude at the cluster redshift. This is done with the EZGAL code (Mancone & Gonzalez 2012a), taking as input the Bruzual & Charlot (2003) population synthesis model with metallicities of $Z/Z_{\odot} \sim 1$ (Mancone & Gonzalez 2012b). The model is calibrated normalizing the model magnitudes to the median observed values, at a redshift $z \sim 0.15$.

The procedure first extracts the galaxies with an r-band magnitude brighter than m_*, and at the same time with $|p_{\rm memb} - p^{\rm max}_{\rm memb}|/p^{\rm max}_{\rm memb} < f_p$ to remove bright, foreground galaxies not belonging to the cluster; $f_{\rm p}$ is a constant whose value is assigned as described below, $p^{\rm max}_{\rm memb}$ is the highest value of the membership probability in each cluster. We then further select those galaxies whose distance from the AMICO cluster centre ($\mathbf{x}$) is within its uncertainty in angular position, $\Delta\mathbf{x}$: as described in Maturi et al. (2019), $\Delta\mathbf{x}$ is a function of the cluster redshift, decreasing from ∼3 arcmin at $z < 0.1$ to ∼0.35 arcmin at $z > 0.45$. These galaxies are then sorted in decreasing membership probability. The BCG is defined as the brightest galaxy in the r band among the first five sorted galaxies; if the difference in magnitude between the first two brightest galaxies is lower than ±0.1 mag, the galaxy with the highest membership probability is selected. If there is no galaxy within $\Delta\mathbf{x}$, we extend the search to $2 \times \Delta\mathbf{x}$, and so on up to a maximum distance of $5 \times \Delta\mathbf{x}$. The second brightest galaxies selected in the same way is also stored, to compute the cluster magnitude gap.

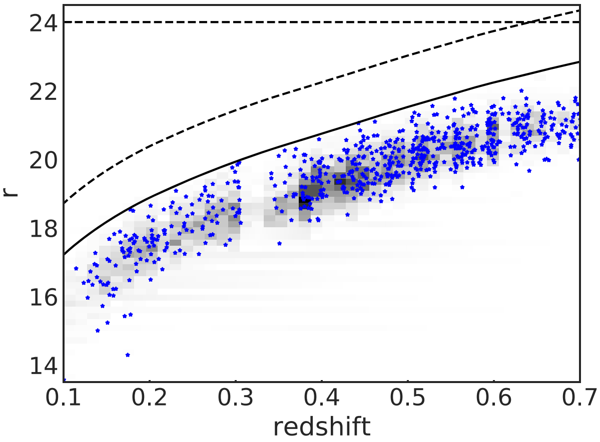

Figure 1. r-band apparent magnitudes of the BCGs (blue dots display late-type BCGs). The solid curve shows the m_* values adopted as a lower brightness limit for the BCGs. The dashed curve ($m_* + 1.5$) is the lower limit adopted for the selection of member galaxies in the present analysis; the dashed horizontal line is the cut ($r = 24$ mag) adopted to select galaxies in AMICO. The gap at $z \sim 0.35$ corresponds to the redshift interval with a reduced coverage of features in the spectral energy distribution by the *ugri* filters, as discussed in Maturi et al. (2019).

To find the optimal choice for $f_{\rm p}$, we proceed as follows. The value of $f_{\rm p}$ is varied between 0.05 and 0.9, and each time the BCGs are identified as described above. Their positions are matched to the GAMA-DR3 catalogue (Baldry et al. 2018), producing $N_{\rm BCG,sp}$ galaxies with GAMA or SDSS spectroscopic redshifts. We then discard those BCGs with a spectroscopic redshift, $z_{\rm sp}$, non-compatible with the one of the cluster detection, $z_{\rm cl}$, i.e. with $|z_{\rm cl} - z_{\rm sp}|/(1 + z_{\rm sp}) > 0.1$, obtaining $N^*_{\rm BCG,sp}$ galaxies. The fraction is $f_{\rm BCG,sp} = N^*_{\rm BCG,sp}/N_{\rm BCG,sp}$. The result is displayed in Fig. 2, showing that an increase in $f_{\rm p}$ produces more BCGs with spectroscopic redshifts (higher $N_{\rm BCG,sp}$), but also more mismatches between spectroscopic and cluster redshifts (lower $f_{\rm BCG,sp}$). We defined $f_{\rm BCG,sp} = 0.9$ as a threshold, which is reached when $f_{\rm p} = 0.2$. This is the value for $f_{\rm p}$ adopted in the following analysis.

3.3 Validation of the membership probability

Spectroscopic redshifts are also used to validate the AMICO membership probability. Since for each cluster few (<10) members with spectroscopic redshifts are expected to be found, to this end we make a stacked analysis (see e.g. Rozo et al. 2015) comparing the average spectroscopic and AMICO membership probabilities for the sample of clusters with spectroscopic redshifts. The spectroscopic membership rate is derived with the following approach:

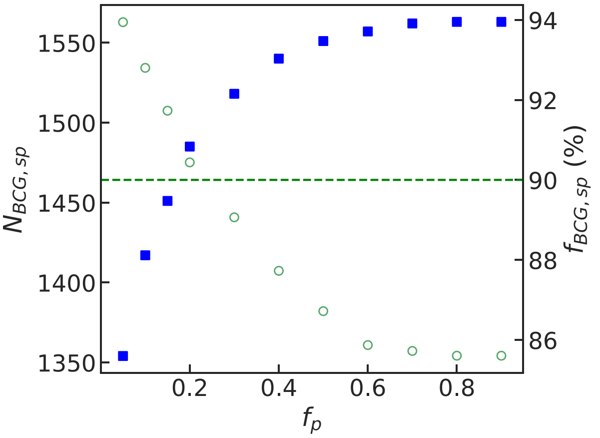

Figure 2. The plot displays, for different values of $f_{\rm p}$: *filled squares* – the number of BCGs with spectroscopic redshifts, left axis); *empty circles* – the fraction of BCGs with cluster redshifts in agreement with spectroscopic redshifts as defined in the text ($f_{\rm BCG,sp}$, right axis). The dashed line is the threshold fraction adopted to select the optimal values of $f_{\rm p}$.

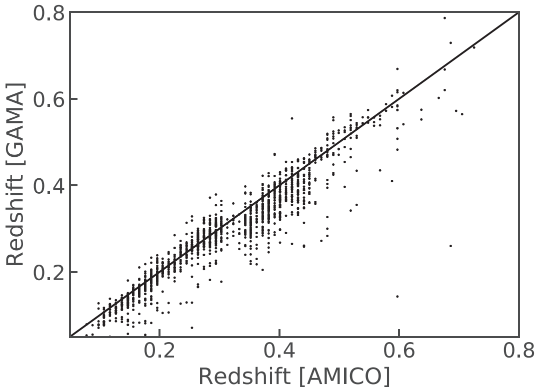

Figure 3. Comparison of AMICO and spectroscopic (GAMA/SDSS) redshifts for the galaxies identified as the BCGs. The solid line displays the 1-to-1 relation as a reference.

(i) We select the ∼1400 clusters for which it is possible to assign a spectroscopic redshift to the galaxy identified as the BCG: this value is adopted as the *initial* cluster redshift ($z_{\rm sp,0}$). Fig. 3 compares this redshift with the AMICO cluster redshift.

(ii) For each cluster, we select all galaxies with spectroscopic redshifts ($z_{{\rm sp},i}$), within a distance of 0.5 h^{-1} Mpc and 5 arcmin from the AMICO cluster centre. *Spectroscopic members* are defined as galaxies with a velocity offset $|\frac{z_{{\rm sp},i}-z_{\rm sp,0}}{1+z_{\rm sp,0}}| < f\sigma_v$, where f is a threshold ($f = 3$) and $\sigma_v = 1500$ km s^{-1} for the first iteration.

(iii) New values of $z_{\rm sp,0}$ and σ_v are computed as the biweight average and standard deviation of the redshifts for these galaxies, and the procedure is repeated until convergence. We verify that the results do not change significantly with different choices of f and the initial velocity dispersion. We finally select ∼760 clusters with at least three spectroscopic members. For these clusters, of the ∼50 000 galaxies for which both a membership probability and a spectroscopic redshift are assigned, ∼ 12 000 are classified as *spectroscopic members* based on the above criteria (the average number of spectroscopic members per cluster is 16).

(iv) The AMICO membership probabilities are binned in steps of 0.05: in each bin we define a spectroscopic membership rate $n_{\rm sp} = N_{\rm mem}/N_{\rm tot}$, and compare it with the AMICO membership probability. Error bars on spectroscopic memberships are obtained by bootstrapping: data are randomly resampled with substitution 10 000 times, spectroscopic memberships are computed and the 5 per cent and 95 per cent percentiles are used as lower or upper limit.[2]

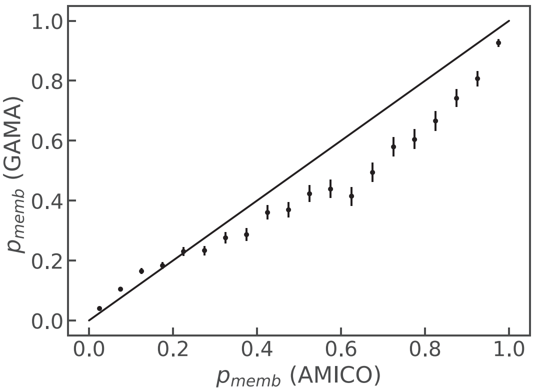

Figure 4. AMICO membership probabilities compared to the fraction of members computed from the galaxies with spectroscopic redshifts. The solid line displays the 1-to-1 relation as a reference.

The results, displayed in Fig. 4, are in good agreement with the comparison with simulated mock catalogues discussed in Bellagamba et al. (2018, fig. 18), where deviations between expected and AMICO membership probabilities are explained by mismatches between the true and model size of the clusters and to miscentrings of the halo positions.

4 RED AND BLUE CLUSTER GALAXIES

Algorithms based on the detection of a red sequence like *redMaPPer* may introduce a bias in estimating the fraction of early- (red) and late- (blue) type galaxies, although they also include blue galaxies as cluster members (see e.g. Groenewald et al. 2017). Since AMICO allows to search for clusters with no assumptions on the colours of their member galaxies, it reduces the risk of introducing such biases. In this section, we describe how blue and red cluster members are selected in the catalogue.

4.1 Classification of red and blue galaxies

Several methods were proposed by different authors to separate *red* and *blue* galaxies in clusters. A method often adopted is to identify the cluster red sequence in the colour–magnitude diagram, and then select as red (blue) galaxies those whose colours are within (outside) a given distance in colour from the red sequence, for instance (see e.g. Pipino et al. 2011) $\Delta = [+0.1, -0.3]$ mag. Andreon et al. (2006) pointed out that this selection introduces a bias due to the evolving colours in redshift, so that at higher redshifts too many galaxies will be classified as *blue*: this may contribute to the so-called Butcher–Oemler effect (Butcher & Oemler 1984), where clusters at increasing redshift are observed to present an increasing fraction of blue galaxies.

---

[2] The same approach is adopted to obtain confidence intervals throughout the paper.

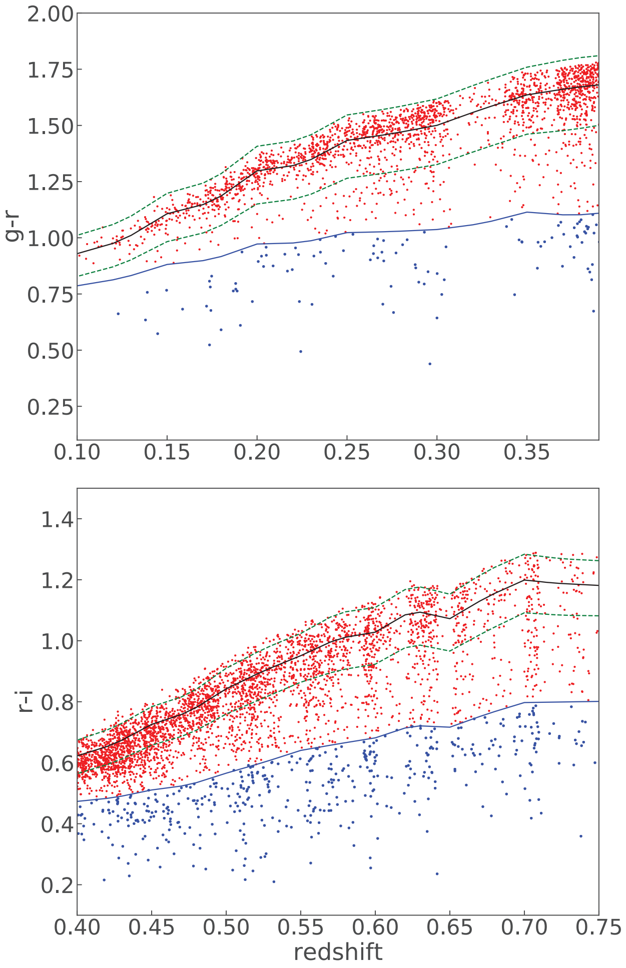

Figure 5. Observed colours of the BCGs are compared to colours for the *E* (red line) and *Sa* (blue line) models defined in the text; the green dashed lines show the elliptical models at metallicities $Z/Z_{\odot} = [0.5, 2]$. ‘Red’ and ‘blue’ BCGs are displayed as red and blue dots, respectively.

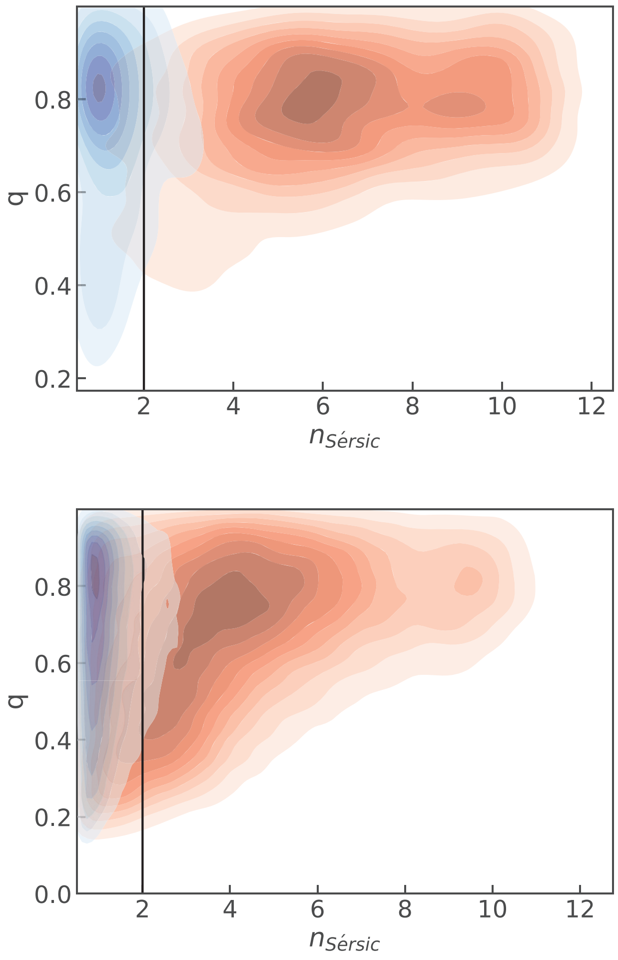

Figure 6. Distribution of the axial ratio (q) and of the Sérsic index for the galaxies classified as blue and red based on their colours. The plot above shows BCGs only, in the plot below all galaxies brighter than $r = 20$ mag are displayed. The vertical line ($n_{\rm Sérsic} = 2$) is the limit adopted to separate red and blue galaxies based on structural parameters.

To avoid this bias, Andreon et al. (2006) proposed two galaxy models based on the Bruzual & Charlot (2003) population synthesis model with solar metallicity, a formation redshift $z_{\rm F} = 11$ and an exponentially declining star formation with e-folding time $\tau = 1$ and $\tau = 3.7$ to describe early (*E*) and late (*Sa*) type galaxies. They then defined as *red* (*blue*) galaxies those *redder* (*bluer*) than an *Sa* galaxy; an upper limit to the colour derived from the *E* model allows to remove those galaxies that are too red at a given redshift to be likely cluster members. Here, we adopt the same approach, using EZGAL to derive the *E* and *Sa* models; the models are calibrated from observed galaxy colours at $z \sim 0.15$. To have a good separation both at lower and higher redshifts, we adopt as colour ($\mathcal{C}$ hereafter) $g - r$ (if $z < 0.4$) or $r - i$ (if $z > 0.4$). We set the upper limit to $\mathcal{C}_E + 0.1$ mag, to take into account the flux uncertainties and the scatter in the colour–magnitude relation due to metallicity (see e.g. Sciarratta et al. 2019). Fig. 5 compares the observed BCG and model colours: to visualize the expected scatter in colours due to metallicity, the model colours from two *E* models at subsolar ($Z/Z_{\odot} = 0.5$) and supersolar ($Z/Z_{\odot} = 2$) are displayed.

As an alternative method, LE PHARE is used to separate the cluster members into red and blue galaxies (see Sarron et al. 2018, for a similar approach). For each cluster, the redshift is fixed to the AMICO cluster redshift, and LE PHARE is run to derive the best-fitting template: we use the CE_NEW library in LE PHARE, which consists of 66 templates based on the CWW (Coleman, Wu & Weedman 1980) SEDs. We define as *red* a galaxy best fitted by a template describing elliptical galaxies, as *blue* otherwise. To improve this morphological classification, we use the nine bands optical + near-infrared photometry available in the KV450 release.

Finally, we also use structural parameters for a classification independent from the colours of the galaxies. From the catalogue of galaxies in KiDS-DR3 with reliable structural parameters ($\chi^2 < 1.3$, $0.5 < n_{\rm Sérsic} < 15$), we select ∼580 000 cluster member galaxies: of these, 2583 are classified as BCGs. Fig. 6 shows the distribution of the Sèrsic index ($n_{\rm Sérsic}$) and axial ratio (q) for the cluster member galaxies classified as blue and red from their colour classification. 2424 are classified as red, 159 as blue, with average values of $n_{\rm Sérsic} = 6.3 \pm 2.1$ and 1.4 ± 1.2, respectively. For bright galaxies, $n_{\rm Sérsic} = 2$ provides a good separation between red and blue galaxies (see e.g. Pandya et al. 2017). However, measurements of the structural parameters for faint and/or high redshift galaxies are hampered by an increasing uncertainty. For this reason in the following discussion on

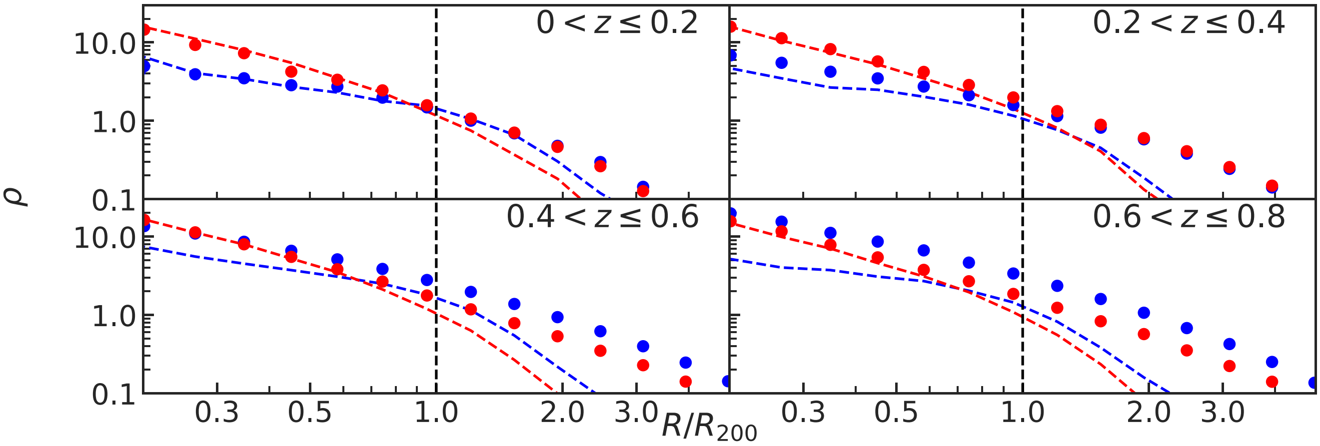

Figure 7. The stacked surface density ($\rho = N/\mathrm{Mpc}^2$) profiles of red and blue galaxies are displayed as a function of the distance from the cluster centre normalized to R_{200}, in different redshift bins. The dashed vertical line marks the position that defines the red fraction (f_r). Dashed curves show the profiles derived from the Illustris TNG300-1 models (see Section 6).

red/blue cluster members we use these results only as a comparison based on a completely independent approach.

4.2 Cluster red sequence

The membership probability and blue/red classification are used together to fit the cluster red sequence. To this end we select galaxies classified as early type, with a probability membership > 50 per cent. We further select the galaxies in the magnitude range $r_\mathrm{BCG} + 0.5 < r < r^* + 2$ to remove the BCGs, which may significantly deviate from the colour–magnitude relation with respect to other cluster galaxies (see e.g. Stott et al. 2009). The fit is done with a robust regression where the Tukey's Biweight function is used as the M-estimator (Venables & Ripley 2002). For both $g - r$ and $r - i$ versus r (observed colours), we are not able to detect any variation of the slope with redshift: for $g - r$, we obtain a slope of -0.04 ± 0.04 in the redshift bin $0 < z < 0.4$ and -0.04 ± 0.08 in the redshift bin $0.4 < z < 0.8$; for $r - i$, the slope is -0.01 ± 0.01 ($0 < z \leq 0.4$) and -0.02 ± 0.04 ($0.4 < z < 0.8$).

4.3 Density profiles of blue and red members

For each cluster, a surface number density profile is derived counting the red and blue members with an r-band magnitude brighter than $m_* + 1.5$, m_* being the characteristic magnitude defined in Section 3.2; each galaxy is weighted by its membership probability, and the resulting number divided by the area of the bin.

To analyse the radial dependence of the density of the red and blue cluster members, stacked surface density profiles are derived by summing the density profiles in different clusters and normalizing over the total number of clusters. The radial profile of the red and blue densities for four redshift bins with a width of $\Delta z = 0.2$ and centred at $z = [0.1, 0.3, 0.5, 0.7]$ is presented in Fig. 7. Here, the distance of the galaxies from the cluster centre is normalized by R_{200}, derived from the AMICO cluster mass (M_{200}, see equation (1)) based on a Navarro–Frenk–White (Navarro, Frenk & White 1997) profile. Within R_{200} the density is larger for red than for blue members: the red/blue ratio decreases with increasing distance from the cluster centre. This is in agreement with what found e.g. by Hennig et al. (2017) and Nishizawa et al. (2018): the value of the cluster red fraction strongly depends on the distance from the cluster centre (see also Wen & Han 2018). We hereafter define as the *red cluster fraction* (f_r) the density ratio of red and blue cluster members within R_{200}.

Fig. 8 displays this fraction for different cluster mass and redshift bins. The same analysis is applied to the blue and red classification derived using colours, the LE PHARE best-fitting templates and the structural parameters; only clusters with a minimum of five member galaxies are selected for this analysis. All classification methods show that the red fraction is ∼70 per cent at low redshifts ($z \sim 0.2$) and decreases (∼50 per cent) as the redshift increases, in agreement with what found in other cluster studies (e.g. Hennig et al. 2017; Sarron et al. 2018; Wen & Han 2018). At redshift $z > 0.4$, the colour and LE PHARE classifications indicate that the red fraction starts to be lower than the blue fraction. In the case of the structural parameter classification, the red fraction still significantly decreases, but not below the blue fraction. The uncertainties are however large, due to the low number of galaxies with meaningful structural parameter measurements: there are ∼40 000 galaxies within R_{200}, compared to the over 450 000 available with the classification based on colours. At redshifts $z > 0.6$ the results are displayed, but the uncertainties are even larger. The red fraction increases for increasing cluster masses, with a steeper increase when $z < 0.4$ and $\log M_{200} < 14$ (see Hansen et al. 2009; Sarron et al. 2018, for a similar result). At higher redshift, the uncertainties do not allow do draw definite conclusions.

To further verify that there is no systematic effect due to how blue/red galaxies are defined, we select a sample of galaxies with a low membership probability ($p_\mathrm{memb} < 20$ per cent): these are more likely to be field galaxies rather than cluster members. For this sample, we find that the red fraction is <0.4 at all redshifts, in agreement with what found by Pandya et al. (2017).

4.4 Comparison with the SDSS-redMaPPer catalogue

Maturi et al. (2019) compared the KiDS-AMICO DR3 and the SDSS *redMaPPer* (v. 6.3, Rykoff et al. 2014; Rozo et al. 2015) cluster catalogues in the redshift range $0.08 < z < 0.55$. They found that 624 (92 per cent) of the 681 clusters detected by *redMaPPer* in the common area (236 deg^2 in KiDS-N) were matched by detections in the KiDS-AMICO catalogue; conversely, 3498 clusters are detected by KiDS-AMICO which are not found by *redMaPPer*. To verify if the unmatched clusters reflect some intrinsic differences in their properties, we first need to account for the different richness cuts

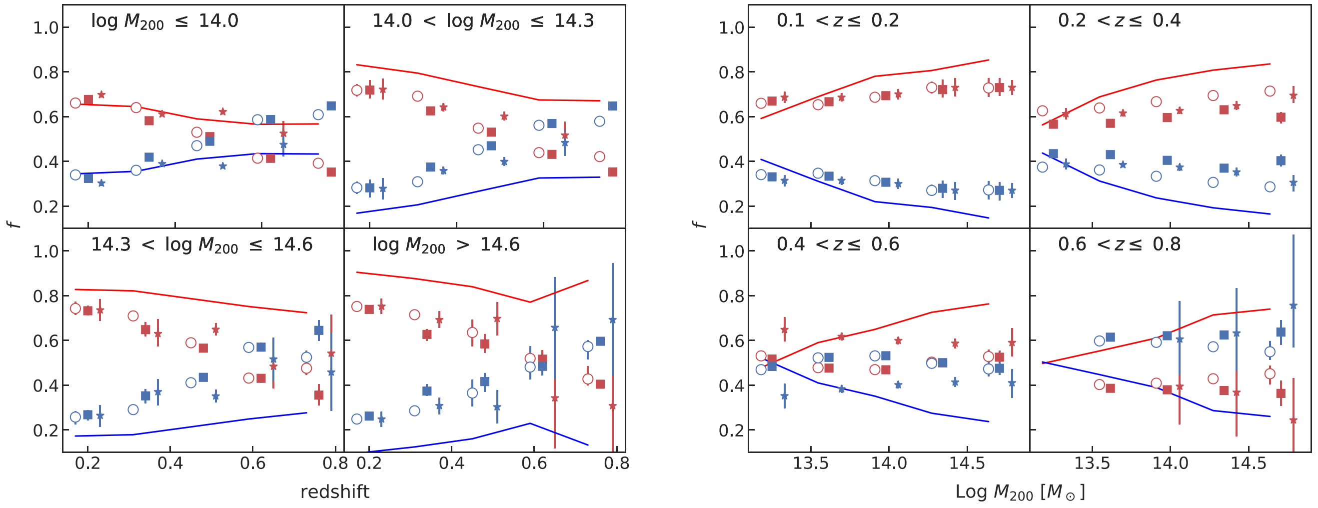

(a) (b)

Figure 8. Red and blue fractions of the galaxies are plotted in bins of (a) cluster mass and (b) redshift: the fractions obtained using the colour, LE PHARE and structural parameter classifications are displayed by circles, squares and stars, respectively; an offset in the x-axis positions was applied to the LE PHARE and structural parameter symbols, for display purposes. The solid red and the blue lines show the values derived using the Illustris TNG300-1 simulations.

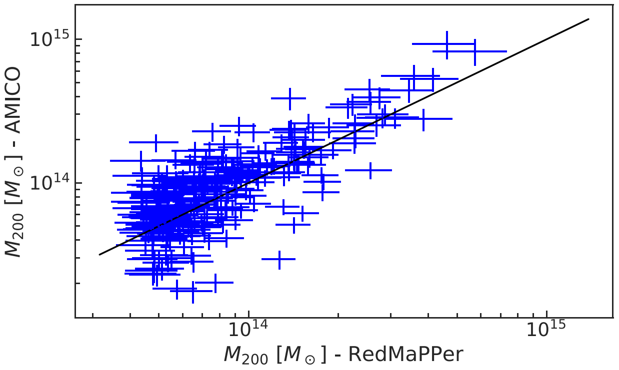

Figure 9. Comparison between masses for matched clusters in the KiDS-AMICO and *redMaPPer* catalogues, in the redshift range $0.1 < z < 0.33$ where the *redMaPPer* mass calibration was done. The solid line shows the 1-to-1 relation as reference.

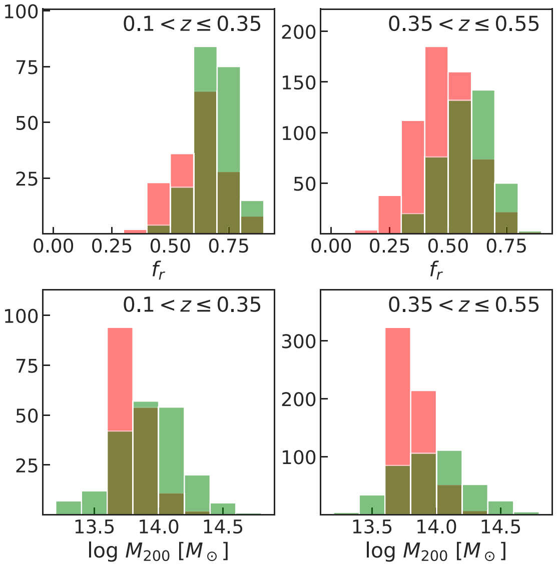

Figure 10. Distribution in fraction of red galaxies ($f_{\rm r}$) and mass (from AMICO) in two-redshift bins for the matched (green) and unmatched (red) clusters from the KiDS-AMICO versus *redMaPPer* catalogues. A cut on mass, $\log M_{200} > 13.5\,{\rm M}_\odot$, was applied to unmatched clusters.

by the two catalogues. Since these are defined in different ways in the two algorithms (SN > 3.5 and $\Lambda_{\rm RM} > 20$ for KiDS-AMICO and *redMaPPer*, respectively), we use the mass derived with the respective scaling relations (Simet et al. 2017; Bellagamba et al. 2019). In *redMaPPer*, the calibration was done using clusters in the redshift range $0.1 < z < 0.33$, and masses were measured within the radius where the mean density is 200 times the mean matter density of the Universe at that redshift ($M_{\rm 200m}$), rather than the critical density as in AMICO ($M_{\rm 200c}$). The conversion from $M_{\rm 200m}$ to $M_{\rm 200c}$ is done assuming a concentration $c_{200} = 4$ (Bellagamba et al. 2019). The masses of matched clusters are displayed in Fig. 9, showing the good agreement between the two estimates, with a median offset $\log M_{\rm 200,RM} - \log M_{\rm 200,AMICO} \sim 0.05$. We finally select only unmatched KiDS-AMICO clusters with $M_{200} > 10^{13.5}\,{\rm M}_\odot$, the lower mass limit in *redMaPPer*, that gives ∼1200 unmatched clusters. Fig. 10 compares the distribution in matched and unmatched clusters of the red fractions ($f_{\rm r}$) defined in Section 4, in two redshift bins: $0.08 < z < 0.35$, where the *redMaPPer* masses were calibrated, and $0.35 < z < 0.55$, where instead the *redMaPPer* masses were extrapolated. There are more unmatched clusters in the high-redshift bin, with lower red fractions ($f_{\rm r} < 0.6$) than at lower redshifts. It should be however noted that 90 per cent of the unmatched clusters have $M_{200} < 10^{14}\,{\rm M}_\odot$: due to uncertainties related to the richness estimate and the mass scaling relations, we are not able to conclude if the unmatched systems are not in *redMaPPer* because of the red-sequence selection on which the method stands, or because their mass is overestimated (underestimated) by the KiDS-AMICO (*redMaPPer*) calibration.

The *redMaPPer* catalogue also lists the five central galaxies, and the one adopted as the cluster centre. For the common clusters, we

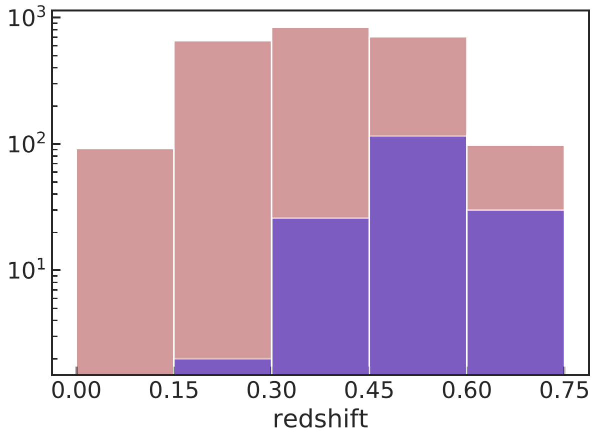

Figure 11. Redshift distribution of red and blue BCGs.

find that for 79 per cent of them the BCG selected in this paper is one of the *redMaPPer* five central galaxies: of these, only 2 per cent are classified here as *blue* BCG. Of the remaining BCGs which are *not* one of the *redMaPPer* five central galaxies, 87 per cent are red and 13 per cent are blue.

5 BCG PROPERTIES

5.1 Blue BCGs

We find that ∼7 per cent of the BCGs are not classified as red galaxies: this fraction is consistent with what found e.g. in the SDSS (Pipino et al. 2011; Cerulo, Orellana & Covone 2019). The redshift distribution for the BCG classified as 'red' and 'blue' is displayed in Fig. 11: the fraction of blue/red BCGs is <5 per cent at $z < 0.3$ and increases to >10 per cent at $z > 0.4$, consistently with Pipino et al. (2011).

5.2 Size and luminosity

To further analyse the BCG properties (BCG stellar mass, size and luminosity) and compare them with the cluster mass (M_{200}), we select a subsample of 2000 BCGs (of which 60 blue) with $M_{\rm star}/{\rm M}_{\odot} > 10^{10.5}\,{\rm M}_{\odot}$ for which measurements of the size are available. The size is the effective radius produced by the fit with the Sérsic profile (see Section 2). The BCG luminosity is the *k*-corrected *r*-band absolute magnitude, where the *k*-correction terms are derived from the LE PHARE output.

Fig. 12 (*top*) shows that there is a correlation between the size and luminosity ($L \propto 10^{-0.4M_r}$) of the BCGs: this is confirmed by the Spearman test, giving a coefficient of 0.5, with a null probability of no correlation. At a given luminosity, red galaxies with a low (<20 per cent) membership probability have a significant smaller size than BCGs at the same luminosity: since field early-type galaxies are expected to have a smaller size than BCGs in clusters (Bernardi et al. 2007; Von Der Linden et al. 2007), this agrees with a higher contamination from non-cluster members as the membership probability decreases. Red cluster members selected to have a more significant membership probability (>50 per cent), but fainter than the BCGs ($r > r_{\rm BCG} + 0.5$) are in an intermediate position. To summarize, we obtain $R_{\rm eff} \propto L^{0.96\,\pm\,0.04}$ (red BCGs), $R_{\rm eff} \propto L^{0.87\,\pm\,0.03}$ (non-BCG red cluster members) and $R_{\rm eff} \propto L^{0.53\,\pm\,0.05}$ (red galaxies with low membership probability). A size–luminosity relation steeper in BCGs than in the bulk of early-type galaxies ($r_{\rm BCG} \propto L_{\rm BCG}^{0.88}$ and $r \propto L^{0.68}$, respectively) was reported by Bernardi et al. (2007). As it concerns blue BCGs, we are not able to derive a significant fit due to their lower number and larger scatter; however, compared to red BCGs their size–luminosity relation appears to be more similar to what measured in galaxies with low membership probability.

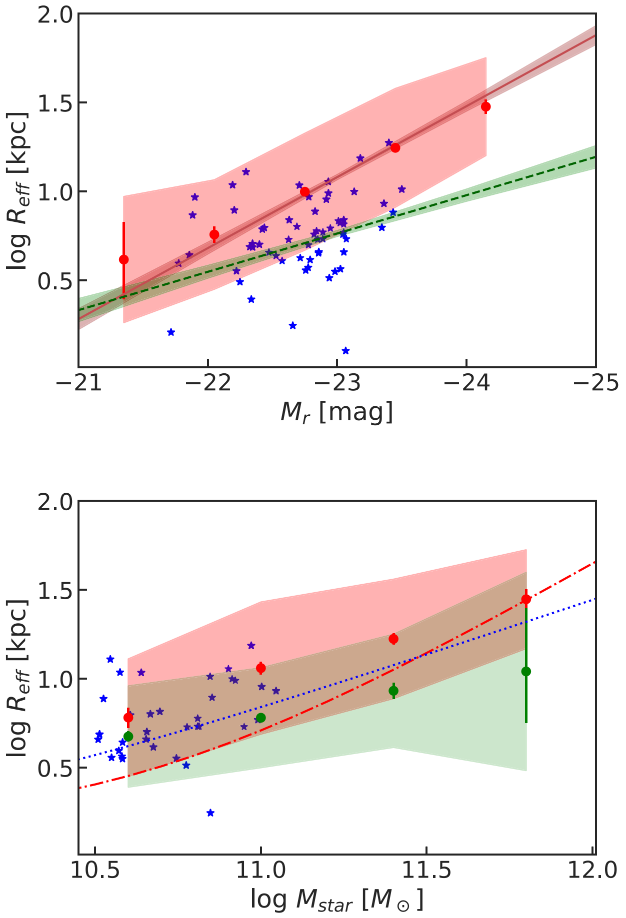

Figure 12. *Top:* size–luminosity distribution in BCGs. The wide area (light red) shows the 1σ scatter for observed values, whose bootstrapped average values and error bars, and linear fits, are plotted in red. Values for blue BCGs are displayed as blue stars. The linear fits for galaxies with a low membership probability are displayed in green; shaded areas display 95 per cent confidence intervals. *Bottom*: the size–stellar mass is displayed for BCGs with $0.3 < z < 0.5$ (same symbols as above) and compared with the fits at $z \sim 0.4$ derived by Roy et al. (2018) for spheroid (dash–dotted red) and disc (dotted blue) galaxies. The wide green area shows the 1σ scatter for low membership probability galaxies.

The existence of a difference in the stellar mass–size relation in clusters with respect to field galaxies, though predicted by hydrodynamical models, is controversial: for instance Huertas-Company et al. (2013a, b) did not find any evidence for differences in the mass–size relation among field, group and cluster galaxies, which was instead detected by Huang et al. (2018). Fig. 12 (*bottom*) compares the values for BCGs in our catalogue with the fits derived by Roy et al. (2018) for spheroid and disc galaxies in KiDS without any selection on the environment, at redshifts $0.3 < z < 0.5$ (similar results are obtained at lower redshifts). The size of red BCGs appears to be larger at a given mass than for other galaxies, though the scatter is large. For stellar masses $M_{\rm star} > 10^{11.5}\,{\rm M}_{\odot}$, the difference is lower, but the

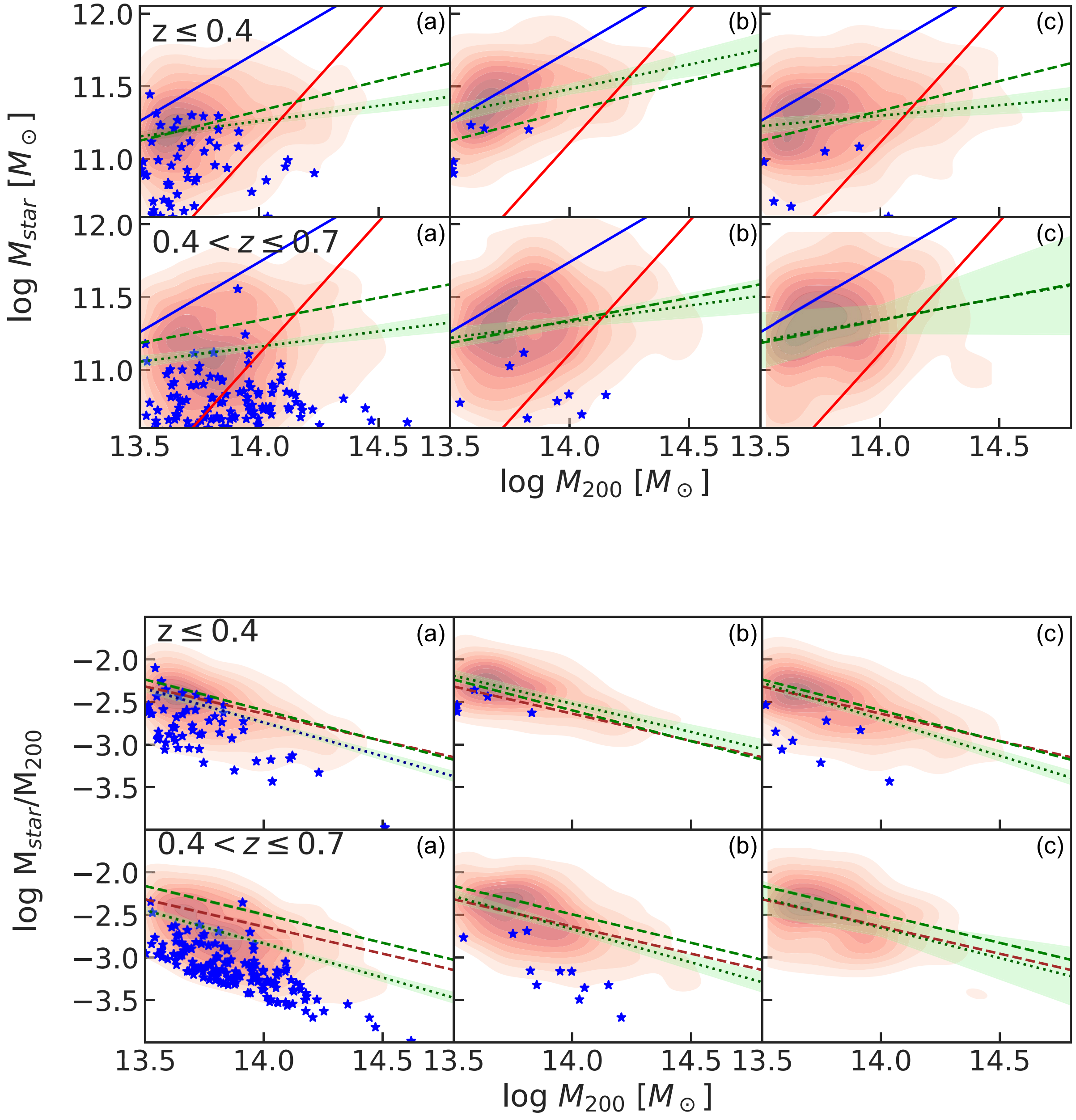

Figure 13. The plots show the distribution of the BCG stellar mass and stellar to cluster mass ratio versus the cluster mass (red contours), with blue BCGs plotted as dark-blue stars. The upper/lower rows show clusters with redshift $z \leq 0.4$ and $0.4 < z \leq 0.7$, respectively, with (from left to right): (a) no selection, (b) $\Delta M_{1,2} > 1$, (c) $f_r > 0.7$. The relations fitted from the data and 95 per cent confidence levels are displayed in green. In the *upper* plots, the blue and red lines display fits derived by Lavoie et al. (2016), weighted to relaxed and unrelaxed clusters, respectively. The dashed green line shows the fit from Erfanianfar et al. (2019). In the *bottom* plots, the red and green lines are the fits derived by Moster, Naab & White (2013) and Girelli et al. (2020), respectively.

sample on which the Roy et al. (2018) fits were derived may be more contaminated by cluster galaxies than at lower stellar masses. Blue BCGs instead, consistently with what already described above, are much closer to the values observed in other galaxies.

5.3 Cluster mass versus BCG stellar mass, and dynamical status

The connection between the BCG stellar mass and the cluster mass is predicted by hierarchical cluster formation models (Hearin et al. 2013; Golden-Marx & Miller 2018, 2019; Farahi, Ho & Trac 2020). We therefore expect to see a correlation (see e.g. Erfanianfar et al. 2019, and references therein) between the cluster mass and the BCG stellar mass, or the stellar to halo mass ratio (SHMR).

Fig. 13 (top) shows the distribution of $\log M_{200}$ versus $\log M_{\rm star}$ for clusters in the two redshift bins ($z \leq 0.4$ and $0.4 < z \leq 0.7$): in both bins, we find a linear correlation between $\log M_{200}$ and $\log M_{\rm star}$, with a moderate correlation coefficient <0.2 given by the Spearman test, and a null probability of no correlation, but with a large scatter. Lavoie et al. (2016) showed that the relation between the cluster and BCG stellar mass depends on the dynamical status of the clusters

Table 1. Coefficients of the fits ($y = mx + c$) for the log $M_{\rm star}$ versus log M_{200} relation, with the different selections (a, b, c) described in Fig. 13.

	m	c	N
$0.1 < z \leq 0.4$			
a	0.21 ± 0.03	8.32 ± 0.38	1551
b	0.34 ± 0.05	6.75 ± 0.73	329
c	0.14 ± 0.04	9.29 ± 0.54	620
$0.4 < z \leq 0.7$			
a	0.21 ± 0.03	8.26 ± 0.43	1789
b	0.22 ± 0.06	8.23 ± 0.81	460
c	0.29 ± 0.17	7.25 ± 2.30	71

(relaxed and non-relaxed): part of the scatter that we observe could be therefore due to the fact that our sample includes clusters in a wide range of conditions. In particular in the lower redshift bin, there is a good agreement between the observed SHMR and the predictions from the models from Moster et al. (2013) and Girelli et al. (2020), which are derived by sub-halo abundance matching models with two different stellar mass functions based on SDSS and COSMOS data, respectively. In our data, at a given cluster mass blue BCGs show lower stellar masses than red BCGs. A similar trend was described by Cerulo et al. (2019), who found a strong decline of the fraction of star-forming BCGs in their sample both with the stellar and cluster mass.

To verify if there is any dependence on the cluster sample selection, in Fig. 13, panels b and c, we show the results of the same analysis performed on clusters with: a magnitude gap, that is the luminosity difference between the two brightest galaxies in the cluster,[3] $\Delta M_{1,2} > 1.0$; a red fraction $f_{\rm r} > 0.7$, to select only clusters where the component of red galaxies is dominant as observed in the low-redshift clusters. The magnitude gap can be used as an indicator of the cluster dynamical status (see e.g. Wen & Han 2013; Lopes et al. 2018), to separate relaxed ($\Delta M_{1,2} > 1.0$) and disturbed ($\Delta M_{1,2} < 1.0$) clusters (Lopes et al. 2018). Consistently, Fig. 13 shows that clusters with $\Delta M_{1,2} > 1.0$ are closer to the position expected from the Lavoie et al. (2016) fits for relaxed clusters, both in the low- and high-redshift bins. Almost no blue BCG with $\Delta M_{1,2} > 1.0$ is observed. In the high-redshift bin, selecting clusters with a low fraction of blue galaxies also moves clusters to the position of relaxed clusters. To have a more quantitative estimate of these dependencies, we show in Table 1 the robust linear fits obtained for each selection, which may be compared e.g. with what obtained by Erfanianfar et al. (2019) for a sample of X-ray selected clusters. Both in the low- and high-redshift bins there is a better agreement with their parameters in the panels denoted with b, suggesting that the dynamical status has indeed to be taken into account.

Fig. 14 compares the magnitude gap with the cluster mass and the BCG stellar mass. The Spearman test gives a correlation coefficient of ~0.4 for the BCG stellar mass, with a null probability of no correlation: systems with larger magnitude gap tend to show a BCG that is more massive. Instead, we see no significant correlation of the magnitude gap with the cluster mass. The same trend is seen in the Illustris TNG300-1 simulations, which are discussed in detail in Section 6. As it concerns blue BCGs, consistently with what discussed above they show lower stellar masses than red BCGs, and a magnitude gap $\Delta M_{1,2} < 1.0$.

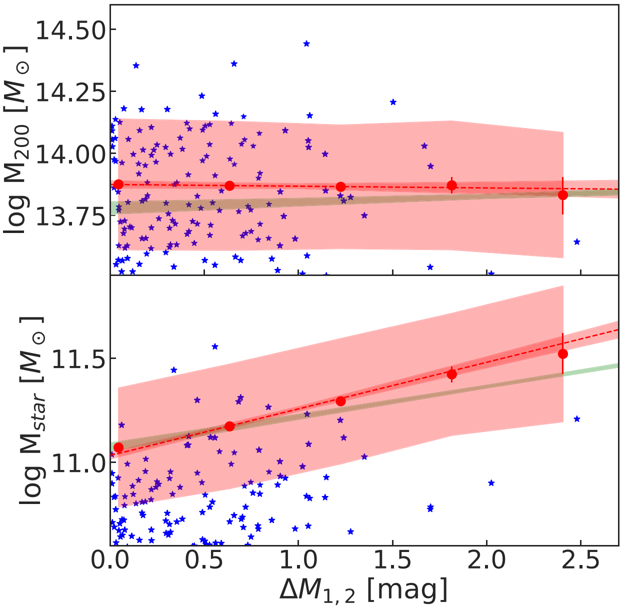

Figure 14. Total cluster mass (top panel) and stellar mass (bottom) as a function of the magnitude gap. The wider area (light red) shows the 1σ scatter for observed values, whose bootstrapped average values and error bars are plotted as red circles. Blue BCGs are displayed as blue stars. The fits derived from the Illustris TNG300-1 simulations are marked in green. Shaded areas display 95 per cent confidence intervals.

Table 2. Definition of the group and subhalo fields from Illustris-TNG, used for the comparison with the observed quantities.

Quantity	Name	Illustris-TNG
Cluster mass	M_{200}	Group_M_Crit200
Cluster size	R_{200}	Group_R_Crit200
Stellar mass	$M_{\rm star}$	SubhaloStellarPhotometricsMassInRad

6 COMPARISON WITH ILLUSTRIS-TNG SIMULATIONS

The Illustris TNG300-1[4] simulations provide 2×2500^3 resolution elements in a volume of $(300\ \mathrm{Mpc})^3$, at 100 redshift snapshots between $z = 0$ and $z = 20$. For each snapshot at redshift $z < 1$, there are ~2500 groups with $10^{13}\ \mathrm{M}_\odot \leq M_{200} \leq 10^{15}\ \mathrm{M}_\odot$, where M_{200} and other parameters[5] from the simulations are defined in Table 2. The BCG in each group is identified as the most massive subhalo. To obtain a sample of simulated clusters matching as close as possible those in the KiDS-AMICO catalogue, clusters from the simulations

---

[3] The magnitude gap is defined here as $\Delta M_{1,2} = M_{r,2} - M_{r,1}$, where $M_{r,i}$ is the k-corrected r-band absolute magnitude of the i-th brightest galaxy.

[4] For more details about the TNG data products, we refer to Nelson et al. (2019) and to the Illustris-TNG website: http://www.tng-project.org/data/docs/specifications/.

[5] As discussed by Weinberger et al. (2017) and Pillepich et al. (2018a), the limited mass/spatial resolutions of the simulations may introduce numerical convergence issues, and as a consequence stellar masses may be underestimated. Comparing TNG300-1 with TNG100-1, where the resolution is higher but the volume is lower, Pillepich et al. (2018b) showed that stellar masses for galaxies in groups and clusters may be underestimated in TNG300-1 by a factor <1.4. Since this does not affect the results in our analysis, we decided to use the original, not rescaled stellar masses.

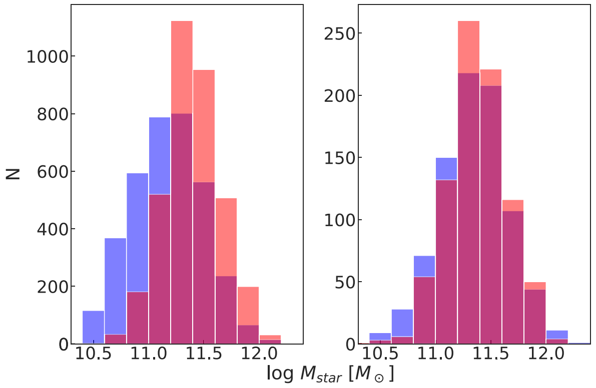

Figure 15. Distribution of BCG stellar masses in KiDS-AMICO (blue), the Illustris TNG300-1 sample (light red). In the *left*-hand panel, the Illustris TNG300-1 simulations are matched in cluster mass and redshift to the KiDS-AMICO subsample with measured BCG stellar mass; in the *right*-hand panel a further selection of clusters with $\Delta M_{1,2} > 1$ is done.

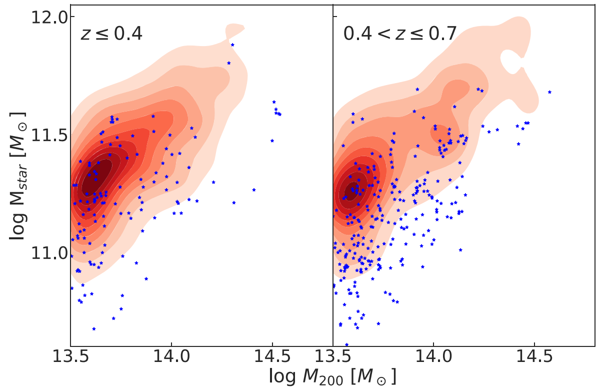

Figure 16. BCG stellar masses versus cluster masses in the Illustris TNG300-1 sample: red contours display the distribution for red BCGs, values for blue BCGs are plotted as blue stars.

are randomly selected so that they reproduce the distribution in mass and redshift of real clusters.

We define the red and blue samples of galaxies in the simulation as we did for the real data, that is according to the $g - r$ ($z \leq 0.4$) and $r - i$ ($z > 0.4$) colours produced by the *E* and *Sa* models. The comparison of the simulated and observed red and blue cluster members should be limited to few R_{200} since the halo finder algorithm adopted in these simulations is designed to identify substructures on scales close to the virial radius (see e.g. Korkidis et al. 2020). Within R_{200}, density profiles (Fig. 7) and red fractions (Fig. 8) show an increasing disagreement for increasing redshift and mass values. Consistently with what we find in our catalogue, the red fraction increases with increasing mass and decreasing redshift. However, while at low redshift (and low cluster masses) the agreement is good, at higher redshift ($z > 0.4$) the simulated red fraction is much higher than what measured in our catalogue. For instance, in the redshift bin $0.6 < z < 0.8$ the blue fraction is higher than the red fraction for all cluster masses in our catalogue, while this only happens for low-mass groups in the simulations.

To compare simulated and measured stellar masses, we repeat the procedure described above, but taking as input the KiDS-AMICO subsample for which a stellar mass measurement is available. The left-hand panel of Fig. 15 compares the distribution of simulated and measured BCG stellar masses, showing an excess of BCGs with measured $\log M_{\rm star}/{\rm M}_\odot < 11$. An improved agreement is obtained further selecting only clusters with $\Delta M_{1,2} > 1$ (Fig. 15, right-hand panel), confirming that clusters with a lower BCG stellar mass are also those with a lower magnitude gap.

Of the simulated BCGs, ∼10 per cent are classified as blue, with a redshift distribution similar to what observed in our catalogue. Based on Tacchella et al. (2019) who analysed morphology, star formation and $g - r$ colours in TNG100 simulations, galaxies with such $g - r$ colours should be mainly disc, star-forming galaxies. Fig. 16 shows the distribution of cluster and BCG stellar masses for the red/blue simulated clusters: they are closer than real clusters (see Fig. 13) to the position occupied by relaxed clusters. Consistently with the observations, also in the simulations the stellar mass in blue BCGs is lower than in red BCGs at a given value of the cluster mass, though the stellar mass of observed blue BCGs is ∼0.2 dex lower than in simulated blue BCGs.

7 DISCUSSION AND CONCLUSIONS

In this paper, we explored the properties (red/blue fraction of BCGs and member galaxies; cluster mass versus the stellar mass, luminosity, and size of the BCG) of galaxy clusters in the KiDS-AMICO (DR3) and their evolution in redshift, based on a catalogue of ∼8000 clusters detected in the 414 deg^2 area covered by KiDS-DR3. Membership probabilities, which are used in our analysis, were validated by the comparison with spectroscopic redshifts available from the SDSS and the GAMA surveys. The comparison with clusters in the SDSS-*redMaPPer* catalogue selected in the same area and in the same cluster mass and redshift range shows that KiDS-AMICO detects more clusters with a lower red fraction than *redMaPPer* and a cluster mass $\leq 10^{14}$ M$_\odot$.

The main results can be summarized as follows:

(i) At low redshifts ($z \leq 0.4$), clusters are dominated by red galaxies; the red fraction and trend with cluster mass and redshift are in good agreement with those obtained from the Illustris TNG300-1 simulations.

(ii) At higher redshifts, the decrease with redshift in the cluster red fraction, implying an increase in the star formation, is much faster in the real data than in the simulations.

(iii) Another disagreement is seen in the cluster mass versus BCG stellar mass distribution: at all redshifts the simulated data are closer to the position occupied in real data by relaxed clusters, while many clusters in the KiDS-AMICO catalogue show evidence for a dynamically disturbed status (low stellar mass at a fixed cluster mass and $\Delta M_{1,2} < 1$).

(iv) In blue BCGs, the stellar mass is lower than in red BCGs for clusters of the same mass: this is also seen in the simulations, though the difference is not as high as in the real data.

The difference in stellar mass between blue (star forming) and red (quiescent) BCGs probably reflects a different contribution by quenching in different cluster environments, in particular by ram pressure stripping (Lotz et al. 2019), with tidal events (Łokas 2020) that may trigger star formation but also deplete the stellar mass.

Based on multiwavelength observations of clusters selected in the South-Pole Telescope Survey, McDonald et al. (2016) found that the fraction of star-forming BCGs is rapidly increasing with redshift, with 20 per cent at $z \sim 0.4$ and ∼90 per cent at z ∼1 showing strong star formation (>10 M$_\odot$ yr^{-1}), and that at $z > 0.6$ they are found in morphologically disturbed clusters. This would be consistent with what we observe in our data, that is blue BCGs are found preferentially in clusters at higher redshifts ($z > 0.4$) and with a low value of the magnitude gap, $\Delta M_{1,2} < 1$, indicative of a disturbed cluster dynamical status. There is evidence (Rodriguez-Gomez et al. 2019) that the Illustris-TNG simulations may not be yet able to fully reproduce gas-rich mergers: this may explain why simulated clusters show properties more typical of relaxed clusters, and as a consequence a lower fraction of star-forming galaxies at increasing redshifts compared to observations.

Work is in progress to extend the cluster detection with AMICO to the next KiDS data releases, that will give an increase in the survey area by a factor of ∼3. At the same time, this will also increase the number of galaxies with measured structural parameters, allowing a more detailed analysis using this classification.

ACKNOWLEDGEMENTS

We thank the anonymous referee for the useful comments that improved the paper.

MS acknowledges financial contribution from contract ASI-INAF n.2017-14-H.0 and INAF ‘Call per interventi aggiuntivi a sostegno della ricerca di main stream di INAF’. CT acknowledges funding from the INAF PRIN-SKA 2017 program 1.05.01.88.04. LM acknowledges the support from the grant PRIN-MIUR 2017 WSCC32 and ASI n.2018-23-HH.0. MR and LM acknowledge the support from the grant PRIN-MIUR 2015 ‘Cosmology and Fundamental Physics: illuminating the Dark Universe with Euclid’.

Based on data products from observations made with ESO Telescopes at the La Silla Paranal Observatory under programme IDs 177.A-3016, 177.A3017, and 177.A-3018, and on data products produced by Target/OmegaCEN, INAF-OACN, INAF-OAPD, and the KiDS production team, on behalf of the KiDS consortium. GAMA is a joint European-Australasian project based around a spectroscopic campaign using the Anglo-Australian Telescope. The GAMA input catalogue is based on data taken from the Sloan Digital Sky Survey and the UKIRT Infrared Deep Sky Survey. Complementary imaging of the GAMA regions is being obtained by a number of independent survey programmes including GALEX MIS, VST KiDS, VISTA VIKING, WISE, Herschel-ATLAS, GMRT, and ASKAP providing UV to radio coverage. GAMA is funded by the STFC (UK), the ARC (Australia), the AAO, and the participating institutions. The GAMA website is http://www.gama-survey.org/. We acknowledge the usage of the Illustris-TNG simulations and of the JupyterLab environment that was made available by the TNG Collaboration to explore and analyse the TNG simulations. We acknowledge the usage of the `StatsModels`, `AstroPy`, `bootstrapped`, `Pandas`, and `Seaborn` libraries in Python.

DATA AVAILABILITY

The data underlying this article will be shared on reasonable request to the corresponding author.

REFERENCES

Aihara H. et al., 2018, PASJ, 70, S4
Andreon S., Quintana H., Tajer M., Galaz G., Surdej J., 2006, MNRAS, 365, 915
Arnouts S., Cristiani S., Moscardini L., Matarrese S., Lucchin F., Fontana A., Giallongo E., 1999, MNRAS, 310, 540
Baldry I. K. et al., 2018, MNRAS, 474, 3875
Barnes D. J. et al., 2018, MNRAS, 481, 1809
Bellagamba F., Maturi M., Hamana T., Meneghetti M., Miyazaki S., Moscardini L., 2011, MNRAS, 413, 1145
Bellagamba F., Roncarelli M., Maturi M., Moscardini L., 2018, MNRAS, 473, 5221
Bellagamba F. et al., 2019, MNRAS, 484, 1598
Benítez N., 2000, ApJ, 536, 571
Bernardi M., Hyde J. B., Sheth R. K., Miller C. J., Nichol R. C., 2007, AJ, 133, 1741
Bertin E., Arnouts S., 1996, A&AS, 117, 393
Blanton M. R. et al., 2003, ApJ, 592, 819
Borgani S., Kravtsov A., 2011, Adv. Sci. Lett., 4, 204
Bruzual G., Charlot S., 2003, MNRAS, 344, 1000
Butcher H., Oemler A. J., 1984, ApJ, 285, 426
Cerulo P., Orellana G. A., Covone G., 2019, MNRAS, 487, 3759
Chabrier G., 2001, ApJ, 554, 1274
Coleman G. D., Wu C. C., Weedman D. W., 1980, ApJS, 43, 393
Dark Energy Survey Collaboration, 2016, MNRAS, 460, 1270
de Jong J. T. A. et al., 2013, The Messenger, 154, 44
de Jong J. T. A. et al., 2015, A&A, 582, A62
de Jong J. T. A. et al., 2017, A&A, 604, A134
De Lucia G., Blaizot J., 2007, MNRAS, 375, 2
Dressler A., 1984, ARA&A, 22, 185
Driver S. P. et al., 2009, Astron. Geophys., 50, 5.12
Erfanianfar G. et al., 2019, A&A, 631, A175
Euclid Collaboration, 2019, A&A, 627, A23
Farahi A., Ho M., Trac H., 2020, MNRAS, 493, 1361
Girelli G., Pozzetti L., Bolzonella M., Giocoli C., Marulli F., Baldi M., 2020, A&A, 634, A135
Golden-Marx J. B., Miller C. J., 2018, ApJ, 860, 2
Golden-Marx J. B., Miller C. J., 2019, ApJ, 878, 14
Groenewald D. N., Skelton R. E., Gilbank D. G., Loubser S. I., 2017, MNRAS, 467, 4101
Hansen S. M., Sheldon E. S., Wechsler R. H., Koester B. P., 2009, ApJ, 699, 1333
Hearin A. P., Zentner A. R., Newman J. A., Berlind A. A., 2013, MNRAS, 430, 1238
Hennig C. et al., 2017, MNRAS, 467, 4015
Hikage C., Mandelbaum R., Leauthaud A., Rozo E., Rykoff E. S., 2018, MNRAS, 480, 2689
Hildebrandt H. et al., 2017, MNRAS, 465, 1454
Hoshino H. et al., 2015, MNRAS, 452, 998
Huang S. et al., 2018, MNRAS, 480, 521
Huertas-Company M. et al., 2013a, MNRAS, 428, 1715
Huertas-Company M., Shankar F., Mei S., Bernardi M., Aguerri J. A. L., Meert A., Vikram V., 2013b, ApJ, 779, 29
Ilbert O. et al., 2006, A&A, 457, 841
Korkidis G., Pavlidou V., Tassis K., Ntormousi E., Tomaras T. N., Kovlakas K., 2020, A&A, 639, A122
Kravtsov A. V., Borgani S., 2012, ARA&A, 50, 353
Kravtsov A. V., Vikhlinin A. A., Meshcheryakov A. V., 2018, Astron. Lett., 44, 8
Kuijken K. et al., 2015, MNRAS, 454, 3500
Kuijken K. et al., 2019, A&A, 625, A2
Lavoie S. et al., 2016, MNRAS, 462, 4141
Łokas E. L., 2020, A&A, 638, A133
Lopes P. A. A., Trevisan M., Laganá T. F., Durret F., Ribeiro A. L. B., Rembold S. B., 2018, MNRAS, 478, 5473
Lotz M., Remus R.-S., Dolag K., Biviano A., Burkert A., 2019, MNRAS, 488, 5370
McDonald M. et al., 2016, ApJ, 817, 86
Mancone C., Gonzalez A., 2012a, Astrophysics Source Code Library, record ascl:1208.021
Mancone C. L., Gonzalez A. H., 2012b, PASP, 124, 606
Marinacci F. et al., 2018, MNRAS, 480, 5113
Martizzi D., Jimmy , Teyssier R., Moore B., 2014, MNRAS, 443, 1500
Maturi M., Bellagamba F., Radovich M., Roncarelli M., Sereno M., Moscardini L., Bardelli S., Puddu E., 2019, MNRAS, 485, 498

Moster B. P., Somerville R. S., Maulbetsch C., van den Bosch F. C., Macciò A. V., Naab T., Oser L., 2010, ApJ, 710, 903
Moster B. P., Naab T., White S. D. M., 2013, MNRAS, 428, 3121
Naiman J. P. et al., 2018, MNRAS, 477, 1206
Navarro J. F., Frenk C. S., White S. D. M., 1997, ApJ, 490, 493
Nelson D. et al., 2015, Astron. Comput., 13, 12
Nelson D. et al., 2018, MNRAS, 475, 624
Nelson D. et al., 2019, Comput. Astrophys. Cosmol., 6, 2
Nishizawa A. J. et al., 2018, PASJ, 70, S24
Oguri M. et al., 2018, PASJ, 70, S20
Pandya V. et al., 2017, MNRAS, 472, 2054
Pillepich A. et al., 2018a, MNRAS, 473, 4077
Pillepich A. et al., 2018b, MNRAS, 475, 648
Pipino A., Szabo T., Pierpaoli E., MacKenzie S. M., Dong F., 2011, MNRAS, 417, 2817
Radovich M. et al., 2017, A&A, 598, A107
Rodriguez-Gomez V. et al., 2019, MNRAS, 483, 4140
Roy N. et al., 2018, MNRAS, 480, 1057
Rozo E., Rykoff E. S., Becker M., Reddick R. M., Wechsler R. H., 2015, MNRAS, 453, 38
Rykoff E. S. et al., 2014, ApJ, 785, 104
Sarron F., Martinet N., Durret F., Adami C., 2018, A&A, 613, A67
Schlafly E. F., Finkbeiner D. P., 2011, ApJ, 737, 103
Sciarratta M., Chiosi C., D'Onofrio M., Cariddi S., 2019, ApJ, 870, 70
Simet M., McClintock T., Mandelbaum R., Rozo E., Rykoff E., Sheldon E., Wechsler R. H., 2017, MNRAS, 466, 3103
Springel V. et al., 2018, MNRAS, 475, 676
Stott J. P., Pimbblet K. A., Edge A. C., Smith G. P., Wardlow J. L., 2009, MNRAS, 394, 2098
Tacchella S. et al., 2019, MNRAS, 487, 5416
To C.-H., Reddick R. M., Rozo E., Rykoff E., Wechsler R. H., 2020, ApJ, 897, 15
Tortora C. et al., 2018, MNRAS, 481, 4728
Venables W. N., Ripley B. D., 2002, Modern Applied Statistics with S, 4th edn. Springer, New York
Vogelsberger M. et al., 2014, Nature, 509, 177
Von Der Linden A., Best P. N., Kauffmann G., White S. D. M., 2007, MNRAS, 379, 867
Wechsler R. H., Tinker J. L., 2018, ARA&A, 56, 435
Weinberger R. et al., 2017, MNRAS, 465, 3291
Wen Z. L., Han J. L., 2013, MNRAS, 436, 275
Wen Z. L., Han J. L., 2018, MNRAS, 481, 4158
Wright A. H. et al., 2019, A&A, 632, A34
York D. G. et al., 2000, AJ, 120, 1579
Zenteno A. et al., 2020, MNRAS, 495, 705

This paper has been typeset from a TEX/LATEX file prepared by the author.